ON THE ANALYTICAL, NUMERICAL AND EXPERIMENTAL MODELS FOR DETERMINING THE MODE SHAPES OF TRANSVERSAL VIBRATIONS OF A CANTILEVER BEAM

Amado ȘTEFAN[1], Andra NEGRU[2], Florina BUCUR[3]

The paper presents theoretical, numerical and experimental aspects regarding the determination of the natural frequencies of transverse vibrations for the beams used in the construction of drones to support the motors. The following schematizations were used: cantilever beam with constant flexural rigidity and rigid mass concentrated at the free end on the beam axis; cantilever beam with constant flexural rigidity, with mass concentrated eccentrically with respect to the axis of the beam at the free end; elastic beam with two intervals of constant rigidity, and eccentrically concentrated mass at the free end. The beam is of an annular section, with the same dimensions throughout the length and is made of carbon fiber composite.

Keywords: transversal beam mode shapes, analytical model, cantilever beam, FEM

1. Introduction

Over the last decades the aviation industry underwent significant changes and unmanned air vehicles are the result of research and evolution in this domain.

An unmanned aerial vehicle (UAV) is an aircraft without a human pilot aboard, commonly referred to as a drone or as an unpiloted aerial vehicle and a remotely piloted aircraft (RPA) [1].

The performance characteristics are important design parameters for the UAVs since the potential drone mission types can be differentiated on their basis. The most important features considered in the design of UAVs include weight, range, endurance, production costs, speed and maximum flight altitude.

UAVs with rotary wings generate the lift from the rotation of the rotor blades [1, 2], which can be designed to have the structure equipped with a number of engines that can vary from one to twelve [3].

The main source of vibration is the rotation of rotor blades assembly and its interaction with air. The natural frequencies of vibrating systems must be different from the frequencies of unbalanced motor rotation and the vortexes frequencies, to avoid resonance regimes.

[1] Assoc. Prof., Ferdinand I Military Technical Academy, Bucharest, Romania, e-mail: amadostefan@yahoo.com
[2] Eng. PhD, Student., Ferdinand I Military Technical Academy, Bucharest, Romania
[3] Lect., Ferdinand I Military Technical Academy, Bucharest, Romania

2. Theoretical approach

The beam model corresponding to the Euler-Bernoulli beam, neglects the effect of the shear force on the displacement of the points on the beam axis, respectively on the rotation angle of the section. Also, the angular acceleration with which the beam element rotates is ignored because in the dynamic equilibrium equation of the beam element the inertia torque is not considered.

The infinitesimal beam element has the mass $dm = \rho \cdot A \cdot dx$, where ρ is density and A stands for the transverse section area.

The inertial force acts in opposite direction with the acceleration of beam element, and it is distributed to the length dx, as in Fig. 1 (T_z and M_{iy} are positive, p_z is positive if it is oriented in positive direction of z axis) .

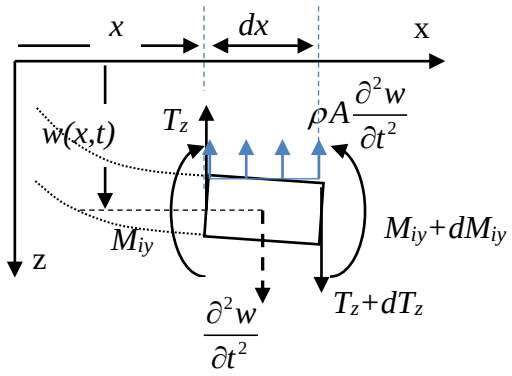

Fig. 1 Infinitesimal beam element

The differential equation of free transverse vibrations under the conditions described above is [4]:

$$\frac{\partial^2}{\partial x^2}\left(EI_y \frac{\partial^2 w}{\partial x^2} \right) = -\rho A \frac{\partial^2 w}{\partial t^2} \tag{1}$$

where $w(x,t)$ is a point displacement along the Oz axis, $\frac{\partial^2 w}{\partial t^2}$ represents the infinitesimal beam element acceleration.

Solution of the differential equation is [5]:

$$w(x,t) = \left(C_1 \sin(kx) + C_2 \cos(kx) + C_3 \sinh(kx) + C_4 \cosh(kx) \right) \cos(\omega t + \varphi) \tag{2}$$

where $k^4 = \frac{\omega^2 \rho A}{EI_y}$, and C_1, C_2, C_3, C_4, ω are the unknowns.

The beam with the motor and accessory parts is illustrated in Fig. 2. The beam section is annular with the outer diameter of 16 mm and the inner diameter of 14 mm and the distance from the clamped end of the beam up to the center of mass of the motor is 273 mm. As for the beam mechanical properties, the Young's

modulus has the value of $3.6 \cdot 10^4$ MPa and density equals 1400 kg/m^3. Because the number of plies and their orientation is unknown, the elastic modulus of the beam is determined using a bending experimental test [6].

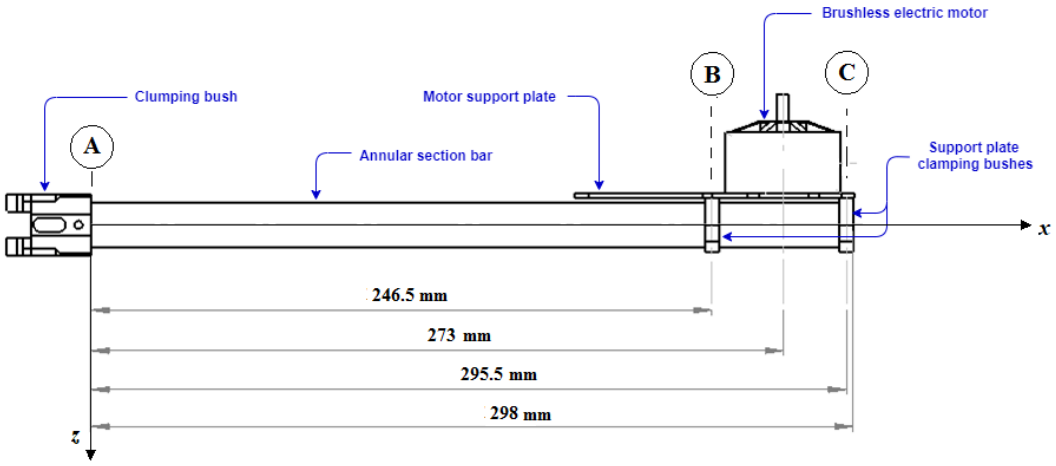

Fig. 2. Geometry of the beam

The following schematizations are used in this research, where section A is fixed (Fig. 3):

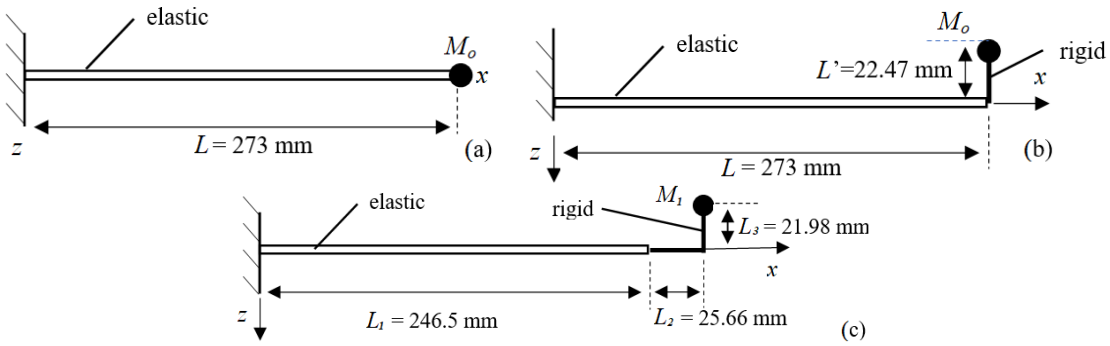

Fig. 3. Considered schematizations for analytical models

For (a) and (b) cases, the mass considered concentrated is the sum of the masses of the clamping bushes, the motor support plate and the motor, respectively 0.143 kg. In case (b), the center of mass eccentricity is at 22.47 mm from the beam axis.

For the (c) case, the beam part between sections B and C (Fig. 2), the clamping bushings, the motor board and the motor are considered rigid. This assumption is made because the motor material is metallic, with a higher rigidity comparative to the beam. The motor support plate weights 1 g. A half of the motor support plate, between section B and C, is rigid because it is clamped and the other half has a free end. The free end half weights 0.5 g so it can be neglected

compared to the motor mass. Fig. 4 shows the part considered rigid and the position of its center of mass relative to section B and the beam axis.

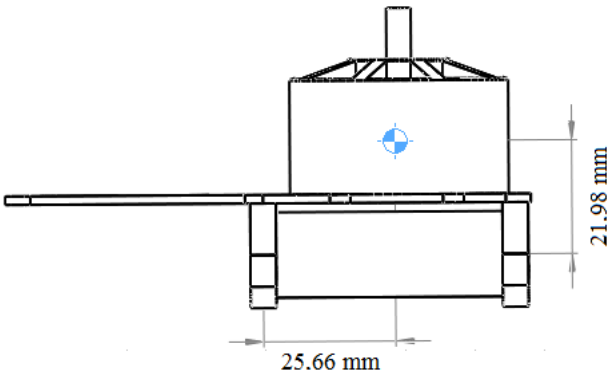

Fig. 4. Part considered rigid

The mass of the part considered rigid is 0.147 kg. The position relative to section B is 25.66 mm through the axis of the beam and to 21.98 mm above it.

In case (a), the integration constants are determined from boundary conditions. In the clamped end of the beam [7]:

$$w(0,t)=0 \tag{3}$$

$$\frac{\partial w(0,t)}{\partial x}=0 \tag{4}$$

and in the free end:

$$T_z(L,t)=-M_0\cdot\frac{\partial^2 w(L,t)}{\partial t^2} \tag{5}$$

$$M_{iy}(L,t)=0 \tag{6}$$

Since $M_{iy}(x,t)=-EI_y\frac{\partial^2 w}{\partial x^2}$ and $T_z(x,t)=\frac{\partial}{\partial x}\left(-EI_y\frac{\partial^2 w}{\partial x^2}\right)$, the following system of four equations with five unknowns is obtained [8]:

$$\begin{cases} C_2+C_4=0 \\ C_1+C_3=0 \\ C_1\left[-EI_yk^3\cos(kL)+M_0\omega^2\sin(kL)\right]+ \\ +C_2\left[EI_yk^3\sin(kL)+M_0\omega^2\cos(kL)\right]+ \\ +C_3\left[-EI_yk^3\cosh(kL)+M_0\omega^2\sinh(kL)\right]+ \\ +C_4\left[EI_yk^3\sinh(kL)+M_0\omega^2\cosh(kL)\right]=0 \\ -C_1\sin(kL)-C_2\cos(kL)+C_3\sinh(kL)+C_4\cosh(kL)=0 \end{cases} \tag{7}$$

Since the system is homogeneous, in order to have a different solution from the trivial one, it must be underdetermined compatible. The system matrix determinant must be null, a condition which represents an algebraic equation with the unknown ω.

The mode shapes (eigenmodes) are represented in Fig. 5, giving the value 1 for C_4 constant and solving the determined compatible system (8), where the constant k is calculated for each mode according to the corresponding pulsation.

$$\begin{pmatrix} 0 & 1 & 0 \\ 1 & 0 & 1 \\ -\sin(kL) & -\cos(kL) & \sinh(kL) \end{pmatrix} \begin{Bmatrix} C_1 \\ C_2 \\ C_3 \end{Bmatrix} = \begin{Bmatrix} -1 \\ 0 \\ -\cosh(kL) \end{Bmatrix} \tag{8}$$

In case (b) and (c) the boundary conditions in the fixed end are similar to those from case (a). At the free end, the shear force equals the mass inertia force, and the bending moment equals the inertia bending moment of the concentrated mass [9].

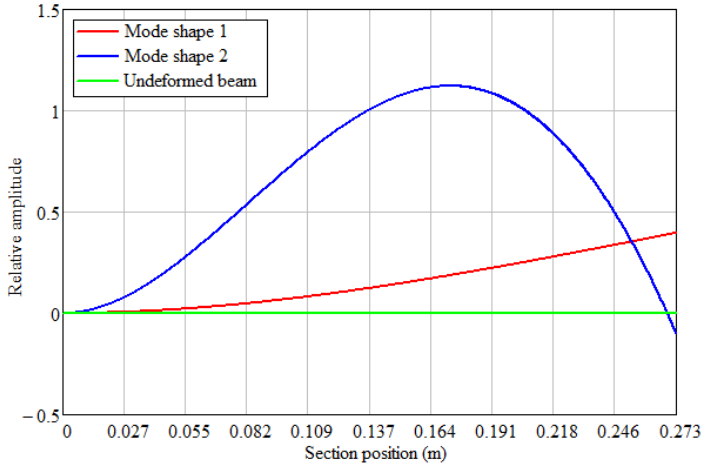

Fig. 5. The 1st and 2nd mode shapes of transverse vibration for case (a)

Thus, for (b) case:

$$T_z(L,t) = -M_0 \cdot \frac{\partial^2 w(L,t)}{\partial t^2} \tag{9}$$

$$M_{iy}(L,t) = M_0 L'^2 \frac{\partial^2 \varphi(L,t)}{\partial t^2} = M_0 L'^2 \frac{\partial^3 w(L,t)}{\partial t^2 \partial x} \tag{10}$$

the equation (7) becomes:

$$\begin{aligned}
&C_1\left[EI_y k^2 \sin(kL) + M_0 L'^2 k\omega^2 \cos(kL)\right] + \\
&+C_2\left[EI_y k^2 \cos(kL) - M_0 L'^2 k\omega^2 \sin(kL)\right] + \\
&+C_3\left[-EI_y k^3 \sinh(kL) + M_0 L'^2 k\omega^2 cosh(kL)\right] + \\
&+C_4\left[-EI_y k^3 \cosh(kL) + M_0 L'^2 k\omega^2 sinh(kL)\right] = 0
\end{aligned} \tag{11}$$

In the schematization from (c) case, the boundary conditions from section B, are:

$$\begin{aligned}
&T_z(L_1,t) = -M_1 \frac{\partial^2}{\partial t^2}\left(w(L_1,t) + L_2\varphi(L_1,t)\right) = \\
&= -M_1 \frac{\partial^2}{\partial t^2}\left(w(L_1,t) + L_2 \frac{\partial}{\partial x} w(L_1,t)\right)
\end{aligned} \tag{12}$$

$$M_{iy}(L_1,t) = M_1\left(L_2^2 + L_3^2\right)\frac{\partial^3 w(L_1,t)}{\partial t^2 \partial x} = M_1 d^2 \frac{\partial^3 w(L_1,t)}{\partial t^2 \partial x} \tag{13}$$

where $L_2^2 + L_3^2 = d^2$ is the distance between section B and the concentrated mass.

The last two relations in system (7) become:

$$\begin{aligned}
&C_1\left[-EI_y k^3 \cos(kL_1) + M_1\omega^2 \sin(kL_1) + M_1 L_2 k\omega^2 \cos(kL_1)\right] + \\
&+C_2\left[EI_y k^3 \sin(kL_1) + M_1\omega^2 \cos(kL_1) - M_1 L_2 k\omega^2 \sin(kL_1)\right] + \\
&+C_3\left[EI_y k^3 \cosh(kL_1) + M_1\omega^2 \sinh(kL_1) + M_1 L_2 k\omega^2 \cosh(kL_1)\right] + \\
&+C_4\left[EI_y k^3 \sinh(kL_1) + M_1\omega^2 \cosh(kL_1) + M_1 L_2 k\omega^2 \sinh(kL_1)\right] = 0
\end{aligned} \tag{14}$$

and

$$\begin{aligned}
&C_1\left[EI_y k^2 \sin(kL_1) + M_1 d^2 k\omega^2 \cos(kL_1)\right] + \\
&+C_2\left[EI_y k^2 \cos(kL_1) - M_1 d^2 k\omega^2 \sin(kL_1)\right] + \\
&+C_3\left[-EI_y k^3 \sinh(kL_1) + M_1 d^2 k\omega^2 cosh(kL_1)\right] + \\
&+C_4\left[-EI_y k^3 \cosh(kL_1) + M_1 d^2 k\omega^2 sinh(kL_1)\right] = 0
\end{aligned} \tag{15}$$

The transcendental equations have been solved using a program with *root function* developed in Mathcad software.

3. Finite element method approach

The CAD model presented in Fig. 2 was developed Solidworks software and analyzed using COSMOSWORKS software.

For the finite element model an automatic mesh was created [10], initially with the average size of elements of 2.5 mm for the support plate, motor and clamping bushes, and 2 mm for the motor support beam. For the beam

discretization SHELL elements with average size of 1 mm and were used. For the other components, SOLID elements were used (Fig. 6).

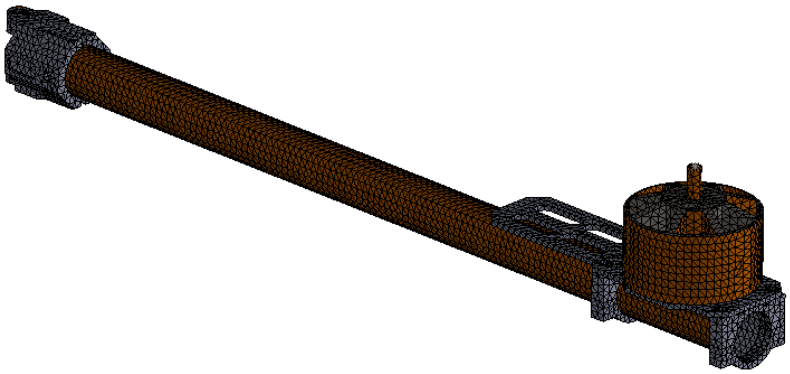

Fig. 6 Finite element discretization

The number of nodes resulted from the discretization are 88845. The clamping bush is restricted in displacement on the surfaces which are in contact with the drone body. The contact between elements is bonded type.

In Table 1 are presented the corresponding frequencies of the first 8 normal modes resulted from the finite element analysis (FEA). The bolded values (from the 1st and 4th mode) are the frequencies that correspond to the first two normal modes of transversal vibrations of the cantilever beam considered.

Table 1

The frequencies for the first 8th eigenmodes of vibration resulted from FEA

Mode number	Frequency (Hz)
1	**36.781**
2	36.951
3	388.86
4	**407.94**
5	485.15
6	659.26
7	1323.5
8	1737.6

In Fig. 7 and Fig. 8 are represented the first and the fourth eigenmode of transverse vibration in plane *xOz* rezulted from the numerical simulations. On the fourth eigenmode of transverse vibration the maximum relative amplitudine is at the free-end of the motor suport plate. The mass of this component is insignificant compared to the mass of the part considered rigid (presented in Fig. 4), for this reason in the analytical study it was neglected.

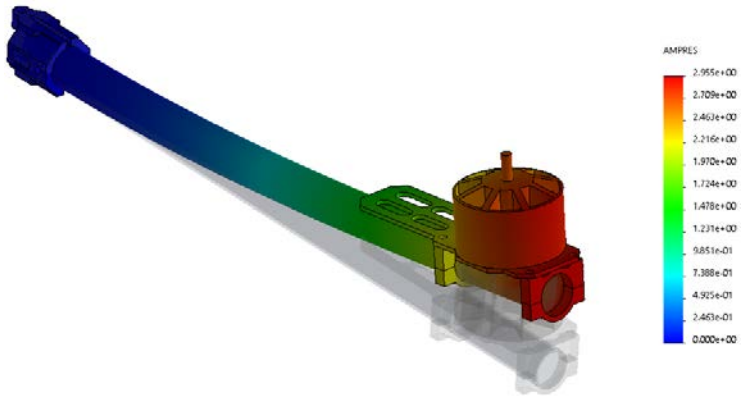

Fig. 7. First mode shape of vibration (first eigenmode of transverse vibration in xOz plane)

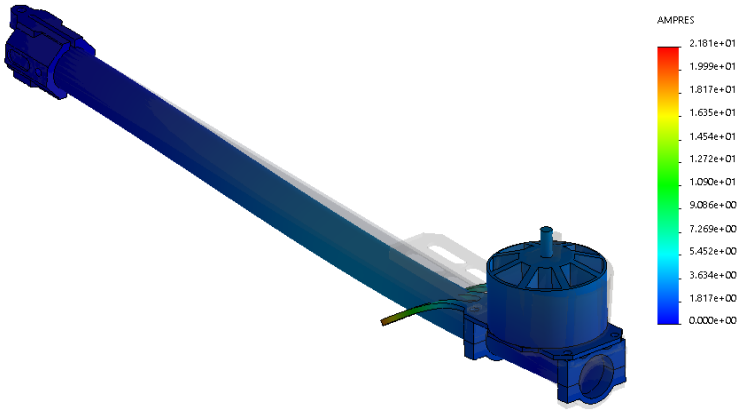

Fig. 8. Fourth mode shape of vibration (second eigenmode of transverse vibration in xOz plane)

4. Experimental results

For the frequency experimental determination of the first eigenmode of vibration, which corresponds to a transverse vibration in the xOz plane, a laser vibrometer Polytec PDV 100 was used, the procedure being similar with the one described in [11]. In Fig. 9 the experimental set-up is presented. The electrical signal acquisition was accomplished with a SIGLENT SDS 1202X-E oscilloscope, which allows storing and measuring the output of the vibrometer (vibrational velocities in the frequency range up to 22 kHz) as presented in Fig. 10. For the excitation of the beam an impact hammer was used. The structure was impulsed in the transversal *Oz* direction, on the motor area.

Fig. 9. Polytec PDV 100 laser vibrometer placed under the electric motor

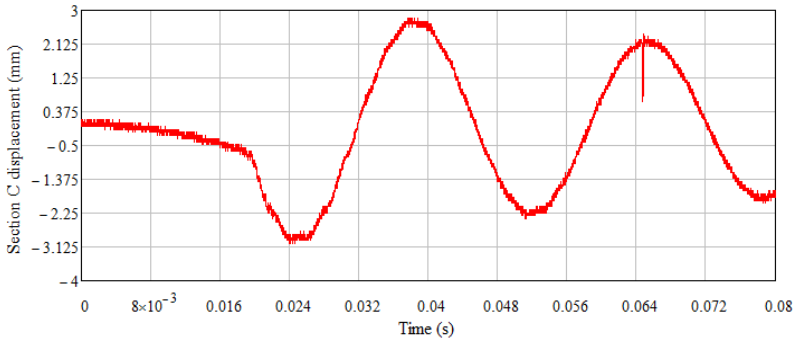

Fig. 10. The signal recorded by the oscilloscope, with the acquisition rate of 100000 Samples/s

Using the Fourier transform of the signal, the 415 Hz frequency was highlighted, corresponding to modes 2 of transverse vibrations in the *xOz* plane. The FFT transform is presented in Fig. 11.

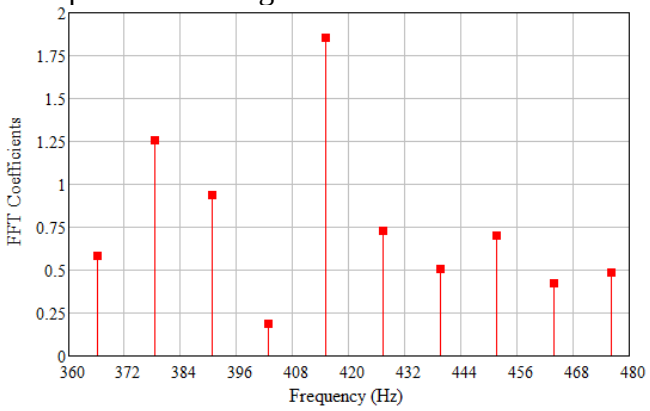

Fig. 11. FFT transform

5. Conclusions and future work

From the finite element analysis were obtained similar results to experimental ones due to the accuracy with which the system geometry is defined (see Table 2 and Table 3). The analytical model in which the motor mass is concentrated on the beam axis, is acceptable for the first mode of vibration, but produces large errors for mode 2 and for higher ones. From all the

schematizations used, (c) case leads to the results closest to the experimental results.

In Table 2, the frequencies corresponding to (a), (b), (c) cases of analytical analysis, FEM and experimental studies are presented.

Table 2

Frequencies (Hz) for (a), (b), (c) analytical cases, FEM and Experimental

Vibration mode	Case a)	Case b)	Case c)	FEM	Experimental
Mode 1	34.50	34.25	36.35	35.20	35.90
Mode 2	890.28	449.96	352.91	407.90	415.00

The percentage errors between the frequency values obtained from experimental and analytical cases, and the ones between experimental and numerical are presented in Table 3. The (a) case of the analytical study has the largest errors compared to the experimental measurement because the inertia moment of the concentrated mass situated on the beam axis is null. The (b) and (c) cases have better results due to moment of inertia calculated with respect to section B, which is different from zero.

Table 3

Percentage errors between experimental-analytical and experimental-numerical values

Vibration mode	Experimental-analytical (a) case (%)	Experimental-analytical (b) case (%)	Experimental-analytical (c) case (%)	Experimental-numerical with FEM (%)
Mode 1	3.87	4.59	1.25	1.95
Mode 2	114.50	8.42	14.96	1.71

In future research, the influence of the rotation frequency of the motor rotor at different speeds acting on the quadcopter arm will be studied. Motor operating regimes which work at a frequency that overlaps the eigen frequency of the beam must be avoided in order to avert the resonance phenomenon.

R E F E R E N C E S

[1]. *R. Austin,* Unmanned Aircraft Systems: UAVS Design, Development and Deployment 54, John Wiley & Sons, 2011.

[2]. *G. Cai, J. Dias, L. Seneviratne,* A survey of small-scale unmanned aerial vehicles: recent advances and future development trends, Unmanned Syst. 2 (02), 175–199, 2014.

[3] *H. Ubaya, M. Iqbal,* First person view on flying robot for real time monitoring, ICON-CSE 1 (1), 41–44, 2015.

[4] *W. Weaver Jr., S. P. Timoshenko, D. H. Young,* Vibration Problems in Engineering, New York D. Van Nostrand company, INC., Second Edition, July, 1937.

[5] *Gh. Buzdugan, L. Fetcu, M. Rades*, Vibrațiile sistemelor mecanice, (Vibrations of mechanical systems), Editura Academiei, 1975. (in Romanian)

[6] ASTM D7264 / D7264M – 15, Standard Test Method for Flexural Properties of Polymer Matrix Composite Materials

[7] *M. Lalanne et. al.,* Mechanical Vibrations for Engineers, John Wiley and Sons Ltd.,1984.

[8] *W. T. Thomson*, Theory of Vibration, Unwin Hyman Ltd. London, 1989.

[9] *L. Bereteu*, Vibrațiile sistemelor mecanice (Vibrations of mechanical systems), 2009. (In Romanian)

[10]. *** COSMOS/M – Finite Element System, User Guide, 1995.

[11]. https://www.polytec.com/fileadmin/d/Vibrometrie/OM_DS_PDV-100_E_42474.pdf